OCT Technique: Past, Present and Future

2

Tigran Kostanyan, Maria de los Angeles Ramos-Cadena, Gadi Wollstein, and Joel S. Schuman

Abbreviations

2D	Two-dimensional
3D	Three-dimensional
AO	Adaptive optics
CCD	Charge-coupled device
EDI	Enhanced depth imaging
FD	Fourier domain
GCC	Ganglion cell complex
ILM	Internal limiting membrane
IPL	Inner plexiform layer
IS	Inner segment
LC	Lamina cribrosa
OCT	Optical coherence tomography
OCTA	Optical coherence tomography angiography
ONH	Optic nerve head
OS	Outer segment
PS	Polarization sensitive
RGC	Retinal ganglion cell
RNFL	Retinal nerve fiber layer
RPE	Retinal pigment epithelium
SD	Spectral domain

T. Kostanyan
Department of Ophthalmology, University of Pittsburgh School of Medicine, UPMC Eye Center, Eye and Ear Institute, Ophthalmology and Visual Sciences Research Center, Pittsburgh, PA, USA

M. de los Angeles Ramos-Cadena · G. Wollstein · J. S. Schuman (✉)
Department of Ophthalmology, NYU Langone Health, New York, NY, USA
e-mail: Joel.Schuman@med.nyu.edu

A. Grzybowski, P. Barboni (eds.), *OCT and Imaging in Central Nervous System Diseases*, https://doi.org/10.1007/978-3-030-26269-3_2

SS	Swept source
TD	Time-domain
Vis-OCT	Visible light optical coherence tomography

2.1 Introduction

Optical coherence tomography (OCT), first developed in the 1990s, is a diagnostic imaging technology that has gained a leading position in research and clinical practice due to its ability to obtain noncontact, in vivo, high-resolution, micron-scale images of tissue structures. OCT makes *in situ* imaging of tissue microstructure possible with a resolution approaching that of histology [1].

The technology uses the principle of low-coherence interferometry, which was originally applied to ophthalmology for in vivo measurements of the axial length of the eye [2].

At the time of introduction, the technology was used to acquire in vivo, cross-sectional images of the anterior segment [3], and retinal pathologies. Since then, OCT has evolved significantly, with improvements in both image acquisition methods and image analysis. The evolution of OCT began with the time domain (TD) technique, followed by spectral domain (SD) systems and later, newer iterations with faster acquisition speeds [4, 5] and improved axial resolution [6].

This chapter describes the basic principles of OCT techniques, its history, current status, major ophthalmic applications, and research that will determine the future of the technology.

2.2 Basic Principles

OCT provides cross-sectional and volumetric images of areas of interest by acquiring either the echo time delay or frequency information of back-reflected light. Differences in the optical properties of biological tissues allow the recognition of layered structures. The speed of light makes it impossible to analyze the acquired information directly, since it would be in the order of femtoseconds thus, OCT systems use the optical technique known as *interferometry*. Low-coherence interferometry enables the analysis of this information and the composition of a depth-resolved reflectivity profile (A-scan) of the scanned tissue by matching the light profiles from the scanning and reference arms.

Utilization of light provides OCT technology the ability to obtain images in a non-contact fashion and to achieve resolutions of 1–15 μm, which is 1–2 orders of magnitude finer than other conventional clinical imaging technologies such as ultrasound, computerized tomography, or magnetic resonance. Light is highly absorbed or scattered in most biological tissues, therefore the use of this technology is limited only to locations that are optically accessible or that can be imaged using devices such as endoscopes or catheters. The eye is the most optically accessible organ of

the human body since the anterior and posterior segments can be visualized and imaged [7].

The key parameters that are typically used to characterize OCT technology are the wavelength of the light source, axial and transverse resolution, scanning speed, and imaging depth.

Axial resolution determines the smallest distance along the axial direction where two adjacent points are discernable, and it is inversely related to the bandwidth of the light source. Current commercial OCT devices achieve axial resolutions up to 4 μm, and research systems can achieve up to ~1 μm [8]. The penetration depth (in the axial direction) is approximately 2 mm in the various OCT iterations with the exception of Visible-light OCT that does not penetrate beyond the RPE layer.

Transverse resolution is determined by the spot size projected into the eye, which is limited by the optical properties of the eye. As such, the transverse resolution of OCT ranges between 15–20 μm among the different generations of the technology. Improving transverse resolution requires the correction of the optical aberrations of the eye using technologies such as adaptive optics.

Scanning speed is dictated by mechanical constrains and the sensitivity of the detector to the back-reflected light. As scanning speed increases, the time the detector remains in the same location is shorter, thus reducing the light that can be detected in each location. Since the power of the projected light is limited in order to be within safety limits, faster scans require a more sensitive detector that can function with a lower level of light.

The achievable imaging depth is related to the central wavelength of the light source, with longer wavelengths providing increased imaging depth [9, 10]. However, longer wavelengths are limited by the increased optical absorption of water [11].

Currently available OCT techniques are based on several iterations of the technology: spectral-domain (SD; also known as Fourier or frequency domain), swept-source (SS), and visible-light (Vis-OCT). The earliest iteration of the technology, time-domain (TD), is no longer manufactured for ophthalmic use and therefore will not be discussed.

SD-OCT uses a broad-bandwidth, low-coherence superluminescent diode laser light that is divided into two arms by a partially reflecting mirror (beam splitter). In the first arm light is projected toward the sampling location, while in the second arm light is projected toward a reference mirror. The backscattered light from both arms travels back to a spectrometer and recombines to form an interference pattern. Light frequency information is analyzed by Fourier transformation to encode distances within tissue microstructure [12]. SD technology allows the acquisition of information from all points along each axial scan (A-scan) simultaneously at a scanning speed of ~25,000–100,000 A-scans/s [13, 14] and up to 20 million A-scans/s in research devices [5]. A cross-sectional image, also known as a B-scan, is generated by performing fast, subsequent A-scans at different transverse positions. Combining rapidly acquired subsequent cross-sectional scans allows the creation of three-dimensional (3D) datasets, enabling advanced post-processing analysis. The wide

bandwidth of the SD-OCT light source also facilitates an axial resolution of 3–6 μm in commercially available systems and up to 1 μm in research systems [15, 16].

SS-OCT uses a tunable laser light source that sweeps through different frequencies in rapid succession to cover the entire broad spectrum. The reflectance of the light from the scanned area is captured by a photodetector, which allows a substantially faster acquisition rate (up to 400,000 A-scans/s) than the spectrometry of SD-OCT [4, 17]. Another important advantage of SS-OCT is an improved signal-to-noise ratio and reduction in the depth dependent signal drop-off observed with SD-OCT technology [18]. Most SS-OCT devices operate with light sources centered at around 1050 nm (compared with 840 nm in the commercially available SD-OCT devices), which reduces the axial resolution to approximately 8 μm but allows for better penetration into the tissue. This combination of improved tissue penetration and reduced signal attenuation allows detailed scanning of structures such as the choroid and the lamina cribrosa (LC) within the ONH.

Vis-OCT. Unlike other OCT iterations that use near infrared light sources (~800 and 1000 nm), Vis-OCT utilizes a light source with a shorter center wavelength of ~550 nm resulting in an improved axial resolution of <1 μm but with reduced achievable imaging depth [19, 20]. Using spectroscopic analysis, it is possible to quantify chromophore concentration from Vis-OCT images [19]. Retinal oximetry is one of its first applications, providing objective, functional information about retinal vasculature. Light absorbance for oxygenated and de-oxygenated hemoglobin peaks in separate wavelengths, both of which are within the spectrum of Vis-OCT. Tissue oxygen consumption can be determined by extracting the venous de-oxygenated level from the arterial oxygenated level. The oximetry information can be aligned to the structural location observed in the same images, opening a new venue for global and local functional assessment.

The major characteristics of these 3 different OCT techniques are presented in Table 2.1.

2.3 The Past

OCT technology was first described by Huang and colleagues in 1991 [21]. The authors scanned human retinas and atherosclerotic plaques ex vivo with a prototype device using infrared light at a ~800 nm wavelength. The axial resolution of cross-sectional images of the retina, optic nerve, and coronary artery wall was 15 μm, which allowed the visualization of some retinal layers, optic nerve head structures, and the composition of the coronary artery. In vivo retinal scanning was conducted using a prototype device based on a slit-lamp biomicroscope that was modified to provide a view of the fundus while scanning with OCT. The development of scan patterns that enabled the acquisition of reproducible measurements [22] led to the use of the technology in clinical practice. The first commercially available OCT, called OCT 1000, was marketed in 1996 by Zeiss (Dublin, CA). The technology went through 2 iterations, resulting in OCT 2000 in the year 2000 and then OCT 3 (Stratus), which became commercially available in 2002. Stratus OCT had an axial

Table 2.1 Comparison of SD-OCT, SS-OCT, and Vis-OCT technologies

Technology	Light source	Primary advantages	Primary disadvantages
SD-OCT	Near infrared broadband width	High scanning speed (up to 100,000 A-scans/s in commercial ophthalmic systems); axial resolution 4–7 μm	Noticeable signal drop-off with depth
SS-OCT	Near infrared narrow bandwidth, swept through broad range	Very high scanning speeds (up to 400,000 A-scans/s in ophthalmic systems); minimal signal drop-off with depth; improved penetration into structures	Most ophthalmic systems operate at longer wavelengths (~1000 nm); with lower axial resolution than SD-OCT (7–8 μm)
Vis-OCT	Center wavelength of ~550 nm from incoherent light sources either spatially coherent or broadband	Highest axial resolution (<1 μm)	Limited penetration into deep tissues; slower scanning speed (up to 30,000 A-scans/s)

resolution of ~10 μm, a transverse resolution of 20 μm, and a scan speed of 400 A-scans/s [1, 23]. The typical cross-sectional scan was composed of 128–512 A-scans, comprising an image area of 4–6 mm.

Due to its ability to obtain quantitative and reproducible measurements of the macula [24, 25], retinal nerve fiber layer thickness [22, 26], and optic nerve head [27], OCT became the gold standard clinical imaging device for posterior segment pathologies in a relatively short period of time.

Early iterations of OCT had a relatively slow acquisition rate, and therefore the conventional scan patterns were comprised of 6 radial scans through the macula (6 mm diameter) or optic nerve (4 mm) with a circular 3.4 mm diameter scan centered on the ONH. Using automated segmentation, the total macular thickness (internal limiting membrane (ILM) to the photoreceptor inner segment-outer segment (IS–OS) junction), retinal nerve fiber layer (RNFL) thickness, and ONH structures were automatically quantified.

The introduction of SD-OCT added a dramatic increase in scanning speed and substantially extended the clinical utility of OCT. The faster scanning speed enabled new scanning patterns such as raster scans, where volumetric data is constructed with a rapidly acquired succession of adjacent B-scans. A 3D dataset allows a thorough sampling of the scanned region, advanced post-processing, and improved registration of consecutive scans. Another commonly used approach is the averaging of consecutive scans acquired at the same location that result in improved image quality.

The majority of commercial OCT systems applied SD technology for posterior eye imaging and visualization of the cross-sectional structures of the retina and optic disc [1] (Fig. 2.1). OCT has been used extensively in the diagnosis and management of a wide range of ocular pathologies including glaucoma, age-related macular degeneration, macular edema, macular holes, diabetic retinopathy,

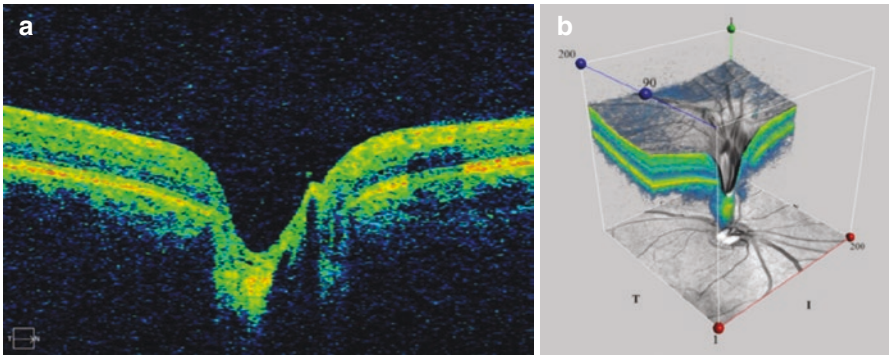

Fig. 2.1 OCT c ross-sectional image of a healthy optic disc (**a**) and a 3D volumetric scan (**b**)

alterations in the vitreoretinal interface, papilledema, and others. In addition to acquiring tissue structural information, OCT has been incorporated into multimodal imaging systems that provide further insight into the functional characteristics of tissue [28–30].

OCT has become a key ophthalmic diagnostic imaging tool due to its ability to provide information about tissue microstructure. Over the years, it has continuously evolved with improved visualization, new retinal imaging locations, increased reliability, and enhanced longitudinal analysis.

2.4 The Present

Since the advent of OCT, 25 years ago, countless improvements have been implemented in an effort to acquire quantitative data with high reliability and sensitivity for precise evaluation of the structure and function of ocular structures.

2.4.1 Spectral-Domain OCT

Since the first FDA-approved SD-OCT became available in 2006, numerous improvements have enriched the capabilities of OCT. One application of advanced processing is the OCT enface image generated by integrating the information from all A-scans into an image of the surface of the retina [31]. The enface image is identical to the retinal fundus view and it can be used for subjective assessment of image quality and eye motion detection, comparison with clinical findings, and further focus on specific location within the region of interest.

Various scan patterns are available for ONH imaging from the different commercially available SD-OCT devices. This includes raster (also known as 3D or volumetric) scans, radial scans, circular scans, and a combination of radial and concentric scans. All of the devices can automatically detect the optic disc boundary as the location at which the photoreceptor layer, retinal pigment epithelium (RPE), and

choriocapillaries terminate. The machine provides quantification of ONH structures such as the disc area, cup-to-disc ratio, and others along with the circumpapillary RNFL thickness measurement reported as global, quadrant, and sectoral thicknesses. Evaluation of the ONH provides important clinical information in multiple ocular and central nervous system pathologies like glaucoma and papilledema.

One of the most useful measurements provided by OCT is the circumpapillary RNFL thickness. Because the axons from the retinal ganglion cells gather to form the optic nerve, a circular scan around the ONH allows sampling of the axons from the entire retina. The limitation of this approach is that the sampling of the tissue is performed only along the circle, therefore any misplacement of the circle during consecutive scanning will result in increased measurement variability [32]. Another option is to extract the RNFL thickness from the raster scan pattern. This method can ensure that the tissue sampling location is consistent through multiple scans, as the repositioning of the circle is possible if needed during post-processing. Several devices also report the RNFL thickness as a color-coded thickness map of the peripapillary region. This map provides additive information to the circumpapillary RNFL thickness measurement, as it can highlight small, localized thinning or defects outside the circumpapillary sampling location. Furthermore, in many devices, the RNFL thickness is compared to population-derived normative data to highlight locations deviating from normal.

Figure 2.2A shows a Cirrus HD-OCT (Zeiss, Dublin, CA) ONH scan printout that provides the RNFL thickness map (a) and cross-section (c). The deviation map (b) compares the RNFL measurements at each superpixel with an age-matched normative database, and locations thinner than the lowest 95% of the normal range are highlighted. In the center panel, quantitative parameters are provided for ONH structures, along with RNFL thickness presented as a thickness profile around the ONH, in quadrants and in clock hours. The background coloring reflects the comparison with the normative database, with green representing the normal range, yellow representing <5% of the normal population, and red representing <1% of the normal population. The right eye shows an example of eye within the normal limits while the left eye shows a glaucomatous eye with thin average RNFL, superior, inferior, and temporal thin RNFL, enlarged cup-to-disc ratio and an inferior notch. OptoVue Avanti (Optovue, Redmont, CA) peripapillary scan (Fig. 2.2B) is created from 13 circular scans with diameters of 1.3–4.9 mm centered on the ONH. Comparison with a normative database is performed in 16 sectors and presented as the deviation map that surrounds the RNFL thickness map. Figure 2.2C shows the circumpapillary RNFL scans obtained with the Spectralis OCT (Heidelberg Engineering, Heidelberg, Germany). A retinal cross section image with delineation of RNFL boundaries is shown in (a). Note the visualization of fine details that is accomplished by averaging repetitive scans acquired in the same location while engaging eye motion tracking systems to reduce motion artifacts. Thickness measurements and color-coded comparison with normative data are presented for global average thickness, quadrants, and in six sectors (b).

The improvements introduced in SD-OCT also have a substantial impact on macular imaging. Thorough sampling of the macula, the improved visualization of the retina and choroid, and the ability to automatically segment the various layers of the retina substantially impacted clinical management. The scan patterns that are

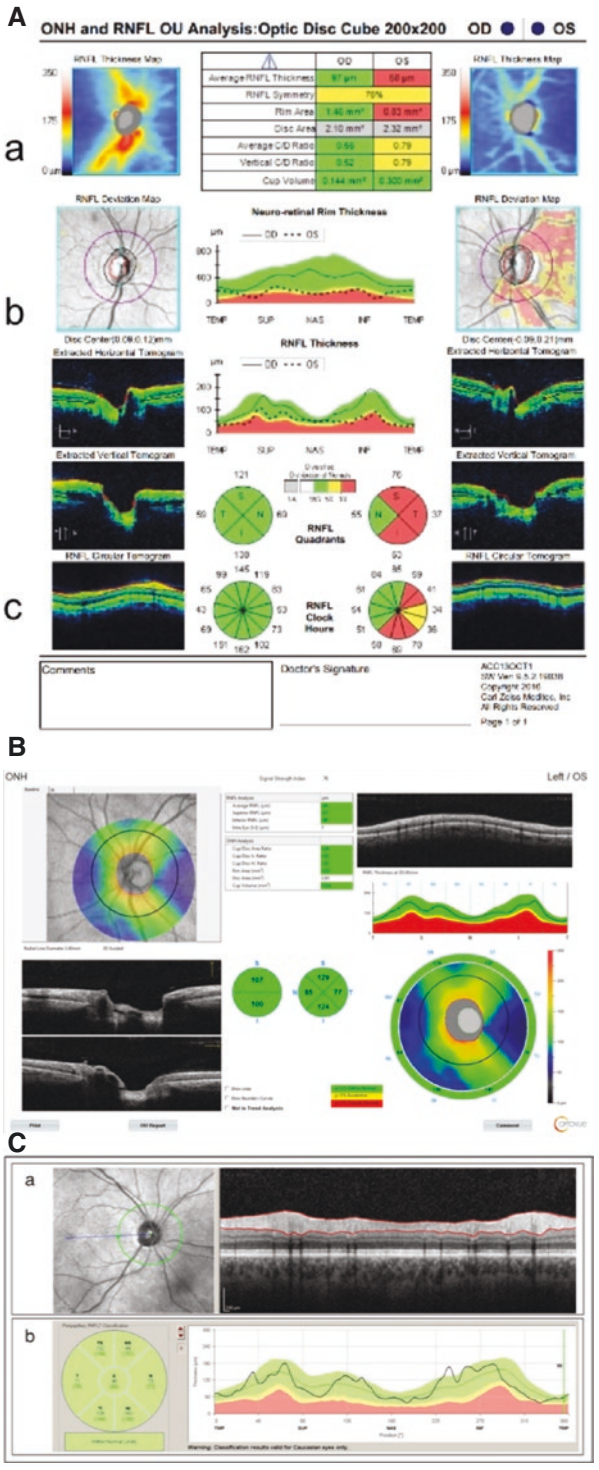

Fig. 2.2 SD-OCT optic nerve head and retinal nerve fiber layer analysis, (**A**) Cirrus, (**B**) Avanti, and (**C**) Spectralis OCT

often used to image the macula include line, cross-line, raster, mesh, and radial scan patterns. Line scans are typically composed from the averaging of multiple scans at the same location. This is typically performed at a single linear location (Fig. 2.3A) or along several parallel lines (Fig. 2.3B). Line scans are clinically useful for obtaining retinal images with the highest level of detail. The principle of the volumetric cube scan is similar to the 3D ONH scan patterns described above. Volumetric macular scans are very helpful in clinical management of macular pathologies, such as macular edema, age related macular degeneration, and macular holes.

Some SD-OCT systems are capable of acquiring scans in horizontal and vertical orientations to provide a mesh scan pattern. The logic behind this scan pattern is that even at a fast scanning rate there is a relatively long temporal gap between adjacent points that are perpendicular to the scan orientation. For example, in a horizontal raster scan, the time gap between adjacent points in the horizontal direction is much shorter than the gap between adjacent points vertically. This can lead to image distortion along the slow axis of the scan. Registering the horizontal and vertical scans together can reduce the distortion in the slow axis and improve scan quality. Figure 2.4 shows the macula thickness map acquired by a retina map scanning pattern (left side of the report) with the correspondent cross-sectional image (right side of the report) obtained with Optovue Avanti (Optovue, Redmont, CA). The pattern consists of an inner, dense grid and outer grid, visible as white grid lines.

Radial scan protocols acquire multiple evenly spaced linear scans that intersect at the fovea. This pattern provides information from the entire macular region, with dense coverage near the fovea where the lines intersect and sparse coverage at the macula periphery. Figure 2.5 demonstrates a radial scanning pattern of the macula from two different healthy subjects using different commercial SD-OCT systems.

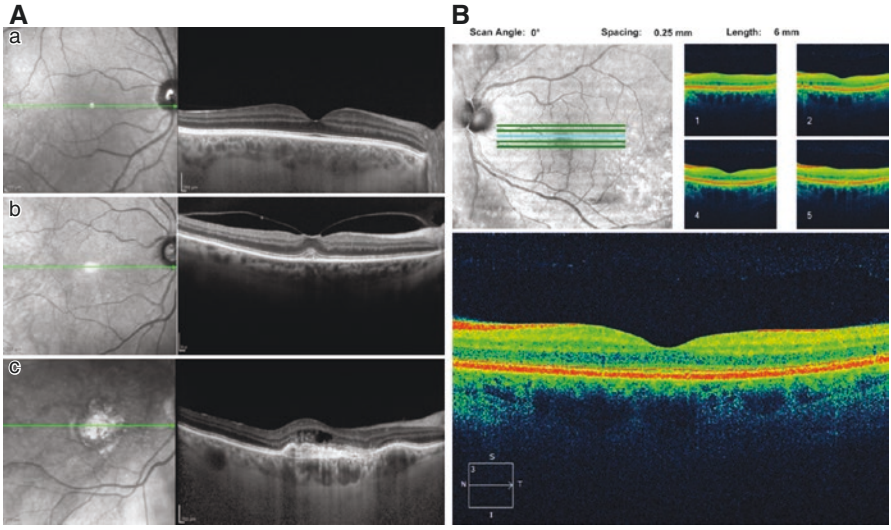

Fig. 2.3 (**A**) Line scans of the macular region obtained with Spectralis OCT from a healthy eye (a), an eye with vitreomacular traction (b), and wet age-related macular degeneration (c). (**B**) Macular five-line raster scan of a healthy eye obtained with Cirrus HD-OCT

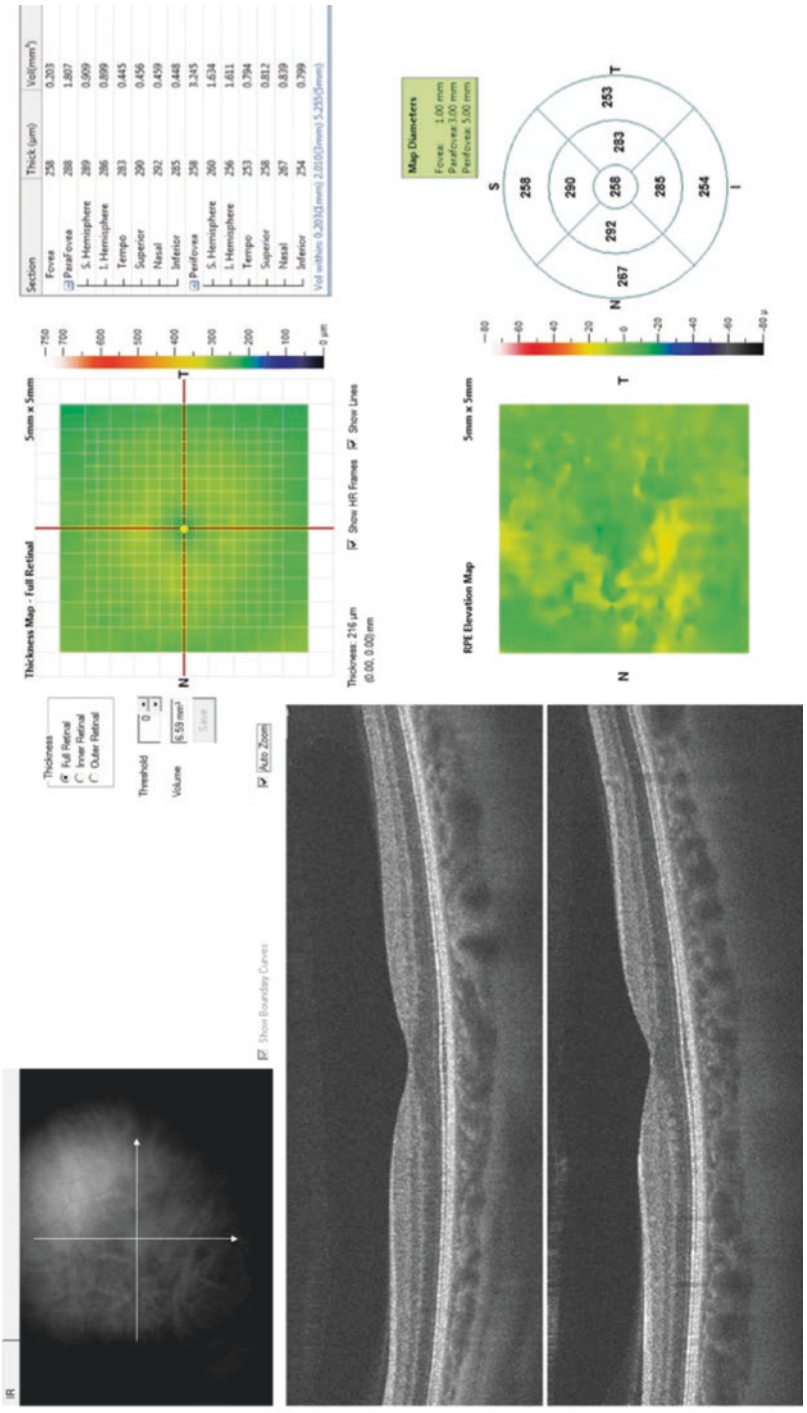

Fig. 2.4 Macular thickness with a retina map scanning pattern obtained with Optovue Avanti

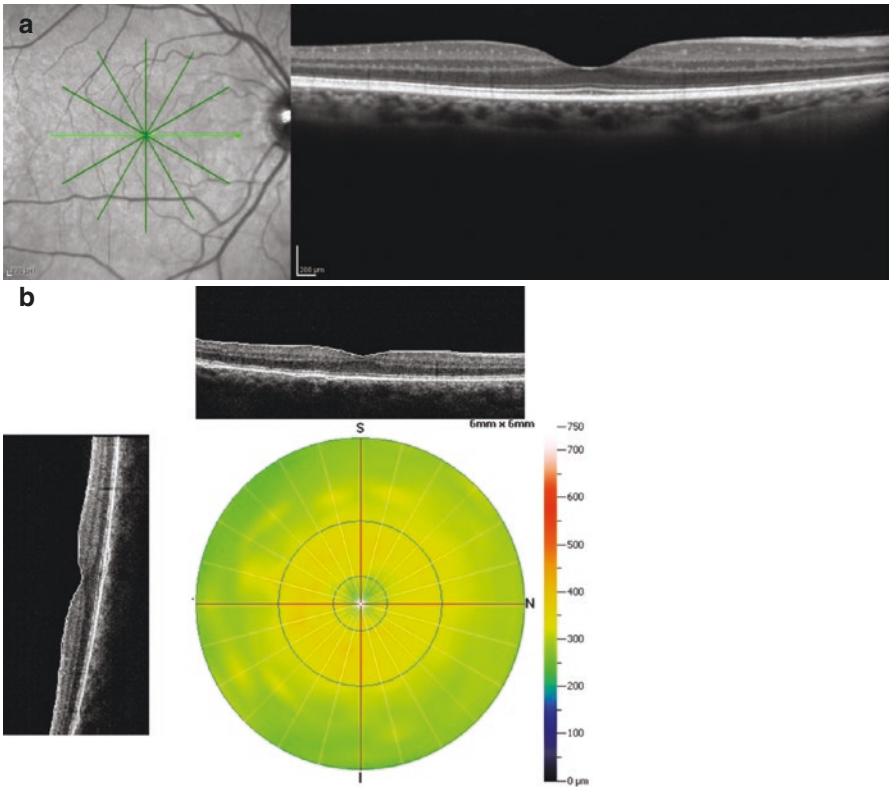

Fig. 2.5 Macular radial scanning pattern obtained with Spectralis OCT (**a**) and RTVue Premier (**b**)

The high resolution of SD-OCT enables automated segmentation and the analysis of individual macular layers that are of particular diagnostic interest in many ocular diseases including glaucoma and diabetic retinopathy [33–35]. Cirrus HD-OCT extracts the information from an ellipse (vertical radius of 2 mm, horizontal radius of 2.4 mm) centered on the fovea and provides a combined measurement of the retinal ganglion cell (RGC) layer and the inner plexiform layer (IPL), called the ganglion cell inner plexiform layer (GCIPL) analysis (Fig. 2.6). The macula protocol of RTVue Premier provides the ganglion cell complex (GCC), which includes the macular nerve fiber layer, RGC layer, and IPL. The data is captured from a 7 mm^2 area centered 1 mm temporal to the fovea.

2.4.2 Retinal and Macular Guided Progression Analysis

The ability of OCT to provide highly reproducible, quantitative, micron-scale measurements is useful in tracking small structural changes that occur over time due to disease deterioration. Several commercial SD-OCT devices include a progression analysis tool. Automatic progression algorithms utilize trend-based analysis

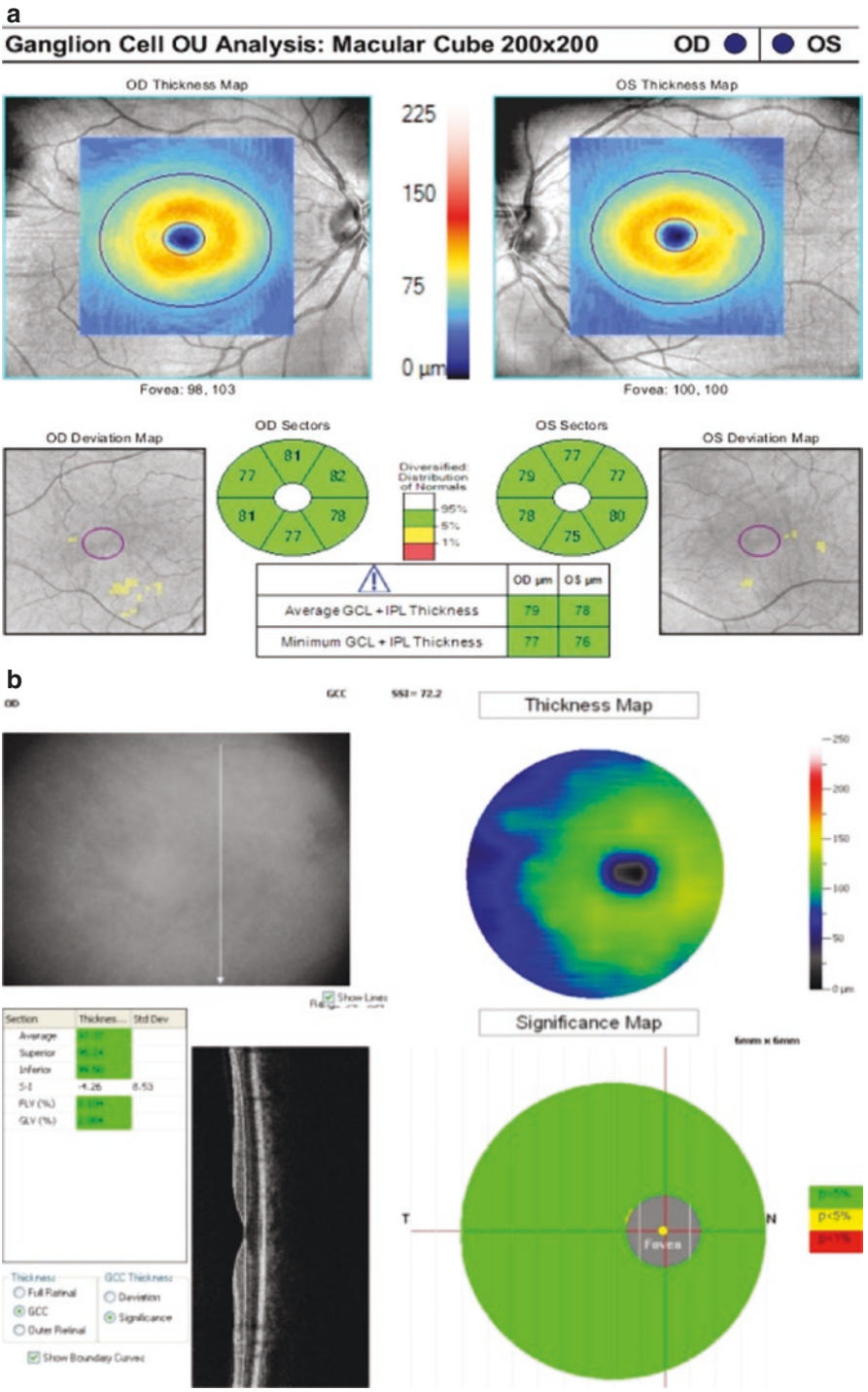

Fig. 2.6 Cirrus HD-OCT ganglion cell analysis (**a**) and RTVue Premier GCC analysis (**b**)

methods, primarily linear regression analysis, for computing the rate of change in structural parameters over time. The computed rate is compared to a no-change slope to determine if the rate is statistically significant. This rate of change is also used to predict future progression beyond the most recent visit. This prediction can be useful when discussing disease forecast with a patient or to assess the effect of treatment modification. Several commercial devices also provide event-based analysis, where a series of follow-up measurements are compared with baseline measurements and progression is defined as measurements changing by exceeding a predetermined threshold from baseline.

It has been described that the peripapillary and macular regions are both capable of detecting glaucoma progression. Glaucoma progression identification has only moderate agreement when looking at these two retinal locations, and different causal theories have been suggested, such as varying dynamic ranges of thickness measurements and minimal measurable thickness (floor effect) with different residual thickness composition (i.e., blood vessels and glial cells), or because one region is affected prior to the other [36–38] .

Figure 2.7 shows the Cirrus HD-OCT guided progression analysis (GPA) for RNFL (A) and GCIPL (B). It provides RNFL and GCIPL event and trend analyses showing a visual display of the location of structural change. In event analysis (a), baseline values are obtained by averaging the data from the first two exams. At least 20 adjacent superpixels must be flagged in the RNFL or GCIPL thickness change maps for a change to be classified as significant. If the difference from baseline is confirmed to be outside the range of test-retest variability, it is classified as "possible loss" and is color-coded in yellow; if the change is confirmed in the subsequent follow-up examination it is classified as "likely loss" and is marked in red. Trend analysis (b) evaluates the rate of change over time using linear regression in the GCIPL, RNFL, and ONH parameters (rim area, average cup-to-disc ratio, vertical cup-to-disc ratio, and cup volume) .

Lately, it was described that macular (GCIPL average, superior, and inferior) and ONH parameters (rim area, cup volume, and cup-to-disc ratio) are sensitive biomarkers to detect glaucoma progression, even in eyes with structural glaucomatous damage, that have reached the floor effect level of RNFL OCT parameters [39] .

2.4.3 Swept Source OCT

At the time of this writing, several SS-OCT devices have been recently approved for use in the USA and worldwide. The major advantages of this OCT iteration compared to earlier ones are the faster scanning speed, deeper penetration into the tissue, and reduced signal attenuation within the scanned window. The counter-effect is a reduced resolution. These properties improve visualization of choroid, sclera, and retinal sub-RPE pathologies such as central serous chorioretinopathy, AMD, choroidal tumors, and retinitis pigmentosa [40, 41]. Examination of the LC and posterior sclera will improve the understanding of the mechanical aspects of glaucoma pathogenesis. Significant differences were documented in the 3D LC

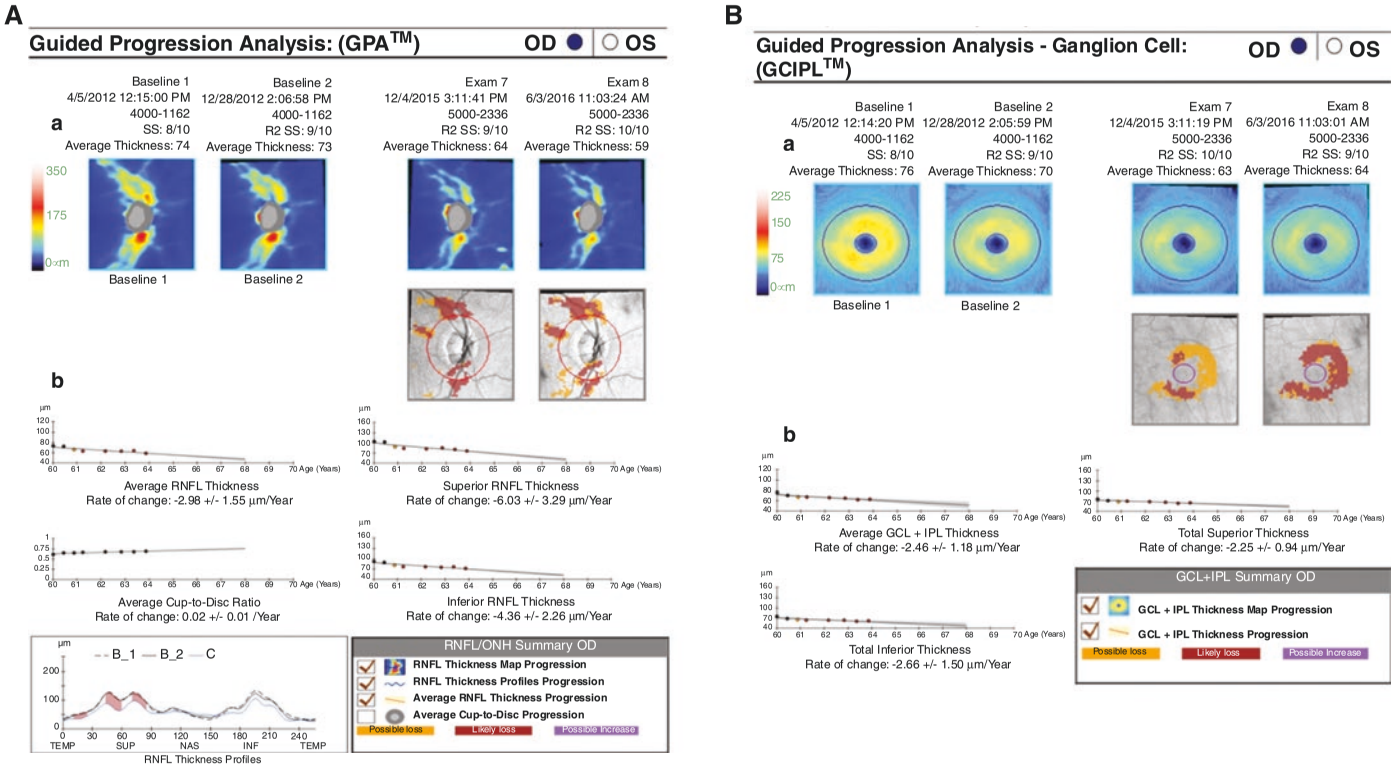

Fig. 2.7 RNFL (**A**) and GCIPL (**B**) guided progression analysis

microstructure between healthy and glaucomatous eyes [42, 43] as well as a more tortuous pathway of the pores in glaucomatous eyes as a potential mechanism for axonal flow obstruction and subsequent damage [44] (Figs. 2.8, 2.9, and 2.10).

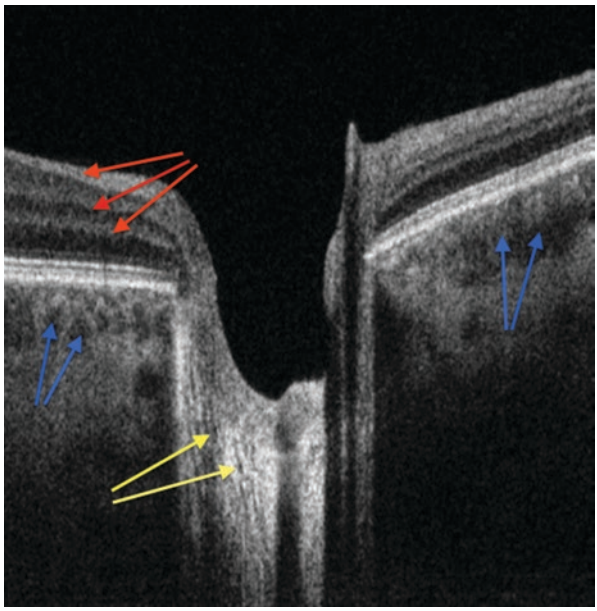

Fig. 2.8 SS-OCT cross section where retinal layers (red arrows), lamina cribrosa (yellow arrows), and choroidal vessels (blue arrows) are all captured in the same scan because this technology is less prone to signal drop-off in comparison with other OCT iterations

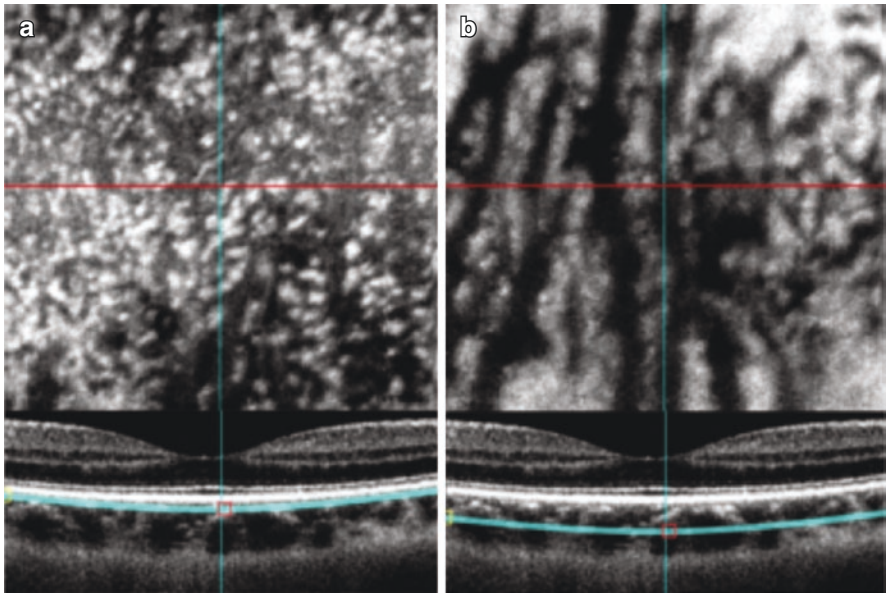

Fig. 2.9 Upper panel demonstrates enface images of SS-OCT of choriocapillaries (**a**) and the large vessels of the choroid (**b**). Bottom panel shows the corresponding cross-sectional scans with the turquoise lines marking the plane where the enface image was acquired

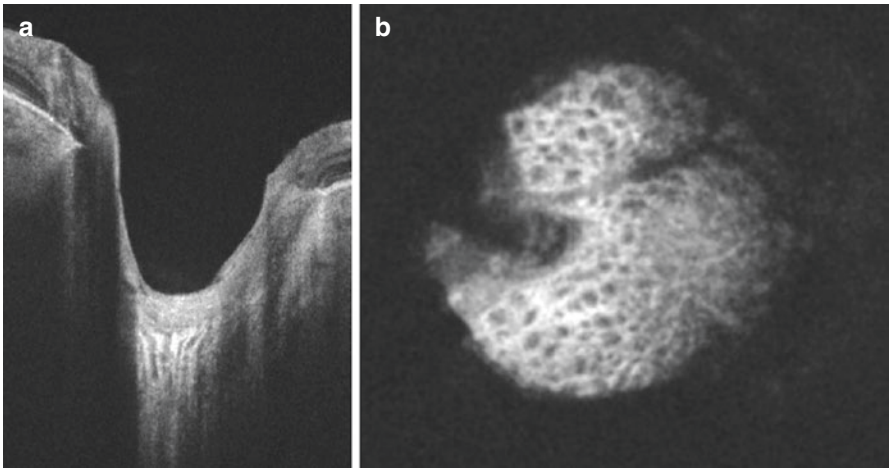

Fig. 2.10 Swept-source OCT cross-section image of the optic nerve head region (**a**). Enface image at the lamina cribrosa level demonstrating the intricate structure of the hyper-reflective beams (white) and hypo-reflective pores (black) (**b**)

2.4.4 Optical Coherence Tomography Angiography (OCTA)

OCTA is an in-vivo, non-invasive, dye-free OCT-based imaging of the blood vessels that provides volumetric vascular analysis [45]. Multiple sequential B-scans are acquired in rapid succession and then compared [41]. The dynamic motion of red blood cells from one image to the other causes a decorrelation signal which is detected by the machine to generate three-dimensional angiograms of the retinal, ONH and choroidal vasculature [41, 45]. It should be noted that this method only provides the anatomical location of blood vessels with flow within a predefined range. Vessels with fast or slow flow outside of this range will not be detected. Furthermore, the device does not report the actual flow within the vessels. The device provides the visualization of blood vessel networks and quantitative analysis of the blood vessel density in the scanned region. OCTA can be performed using both SD-OCT and SS-OCT technologies. At the time of this writing, a few different OCTA are commercially available.

Figure 2.11 shows the SD-OCTA Angioplex report of both ONH and macula angiography scans. The report includes the enface angiography images at different depths on the left, the superficial vascular network and cross-sectional scan overlaid with the location of detected vessels in the middle, and the vessel density analysis by region in the inferior right corner.

Figure 2.12 shows the ONH SS-OCT Triton angiography report. The top row of the report shows the angiography analysis in different depths starting with the innermost section closest to the ILM (labeled as the "nerve head"), followed by an intermediary depth (vitreous), then the analysis at the level of retinal photoreceptor cells (RPC), and ending closest to the choroid (choroid disc). The inferior row shows on the left a cross-sectional image of the optic nerve and in the middle a color-coded vessel density map.

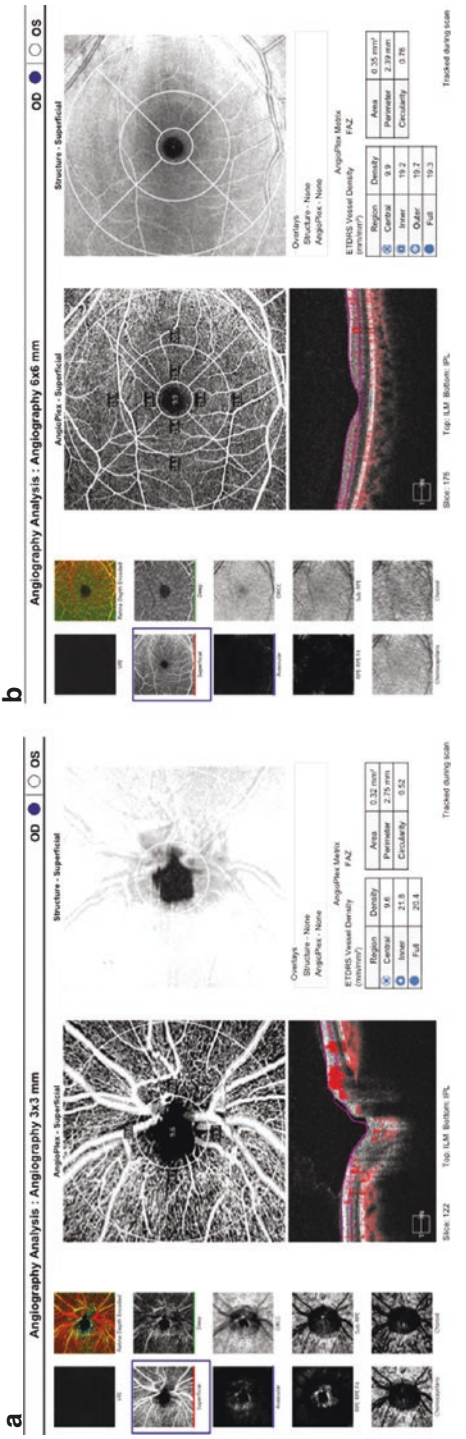

Fig. 2.11 Angioplex angiography with the 3 × 3 ONH (**a**) and 6 × 6 macula (**b**) report

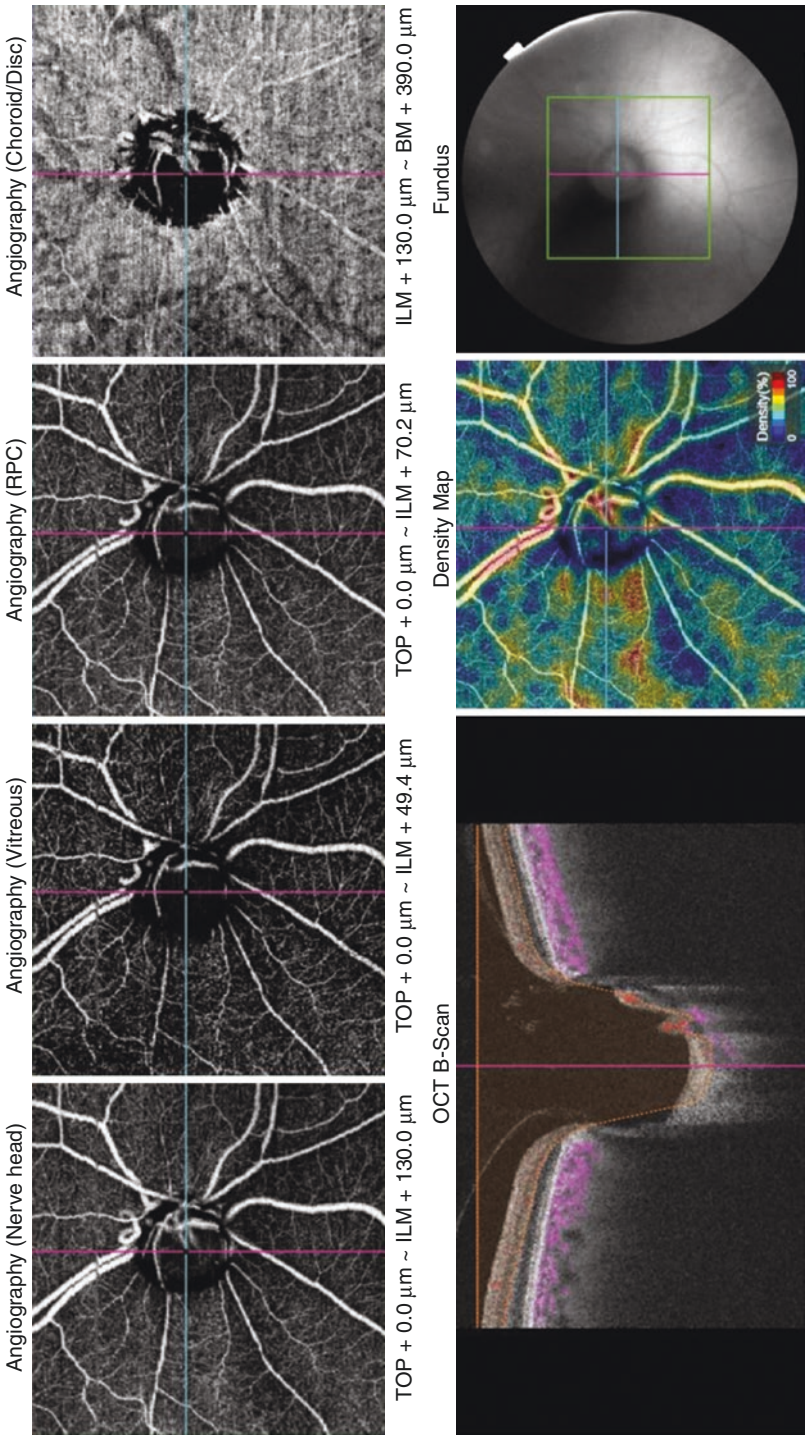

Fig. 2.12 Triton ONH angiography report

2.5 Doppler Optical Coherence Tomography

This technique allow determining arterial and venous blood flow through spectral-domain and swept-source based Doppler OCT [46]. Based on the Doppler shift detected in the OCT signal, this method can determine depth-resolved retinal vessels flow without the use if dye [47]. However, notable drawback of this method are that it cannot detect flow if the vessels are perpendicular to the incident OCT beam or in smaller size vessels [48]. While Doppler OCT retinal blood flow measurements showed good repeatability and excellent correlation with clinical presentations of retinal diseases, the role of this technique in disease detection and monitoring is yet to be determined [48].

2.6 The Future

As technology keeps evolving, several innovative OCT technologies are being tested. The following sections will provide a brief description of some of the most promising developments.

2.7 Adaptive Optics

Adaptive optics (AO) is an optical method designed to dynamically adjust monochromatic aberrations in optical systems. AO was initially used in astronomy for correcting distortions of light passing through the atmosphere. The first in vivo examination of the retina with an AO fundus camera using a wave front sensor and a deformable mirror was introduced in 1997 [49]. A few years later, AO was combined with scanning laser ophthalmoscope [50] and OCT systems [51]. As discussed above, the transverse resolution of all conventional OCT systems is limited to the range of 15–20 μm due to the optical aberrations of light beams when passing through various media in the eye. AO measures and corrects the optical aberrations, reduces the projected spot size, and improves the transverse resolution from 20 μm to the range of 5–10 μm [51]. This resolution allows the acquisition of highly detailed images, enabling the visualization of fine details such as the retinal microvasculature, photoreceptor mosaic [52], LC, and microstructures within the RNFL [6, 53] and ganglion cell layer. The ability to acquire highly detailed in vivo images of these structures allow further insight into ocular anatomy in health and disease, providing the opportunity to expand the understanding of pathologic processes in the eye.

The major limitation of the AO technique is the small field of view, which is restricted to approximately 1°–3°. The use of an eye-tracking system to acquire a series of neighboring scans to cover a larger volume can resolve this limitation, though the longer scanning time might prohibit large scale clinical use [54]. Similarly, the focusing depth of the AO technique is also limited, and therefore acquiring high quality images of thick structures such as the choroid and retina in

the same image is difficult to obtain. It may be possible to address this limitation by varying the focal plane while scanning in depth [55]. The volume of data, needed for image processing, and advanced analysis requirements are also a limiting factors for commercialization of the technology. Datasets are 100 times larger than the conventional OCT counterparts, and therefore storage and accessibility of the information are challenging [56].

2.8 Visible-Light OCT

Switching to light sources in the visible light wavelength (~550 nm), instead of near infrared wavelengths, allows further improvement in axial resolution to the level of <1 μm and the extraction of spectroscopic information that is registered to the structural information. The higher scattering coefficients of biological tissue with visible light improves imaging contrast, but at the expense of reduced imaging depth (Fig. 2.13) [19]. Speckle noise reduction techniques can be applied to reduce background noise level and further improve image quality.

The evaluation of oxygen saturation through spectroscopy analysis is one of the most promising applications of the Vis-OCT system [19]. By taking advantage of the distinct light absorption of oxygenated and de-oxygenated hemoglobin within the visible spectral range it is possible to determine the oxygen consumption of tissue in a given region [20]. The role of oxygen saturation and consumption by the ocular tissue for diagnosing and monitoring various ophthalmic disease is currently being examined. Other chromatophores indicating metabolic and biochemical tissue activity are also being initially evaluated.

2.9 Polarization Sensitive OCT

Polarization sensitive OCT (PS-OCT) uses the polarization state of polarized light for the assessment of tissue function. Different ocular structures and tissues alter the polarization state of light in different ways, such as through birefringence (sclera, RNFL), polarization-preservation (photoreceptors), and depolarization (RPE) (Fig. 2.14). PS-OCT estimates these light state alterations by simultaneously

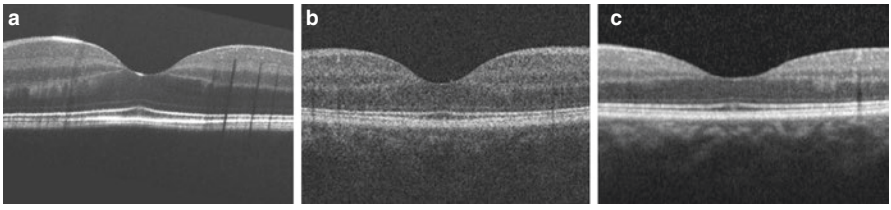

Fig. 2.13 Macula scan of the same subject with Vis-OCT with speckle reduction (**a**) Cirrus OCT (**b**), and Spectralis OCT (**c**). Note the improved visualization with the Vis-OCT and the distinct interface between retinal layers without the need of averaging of multiple images

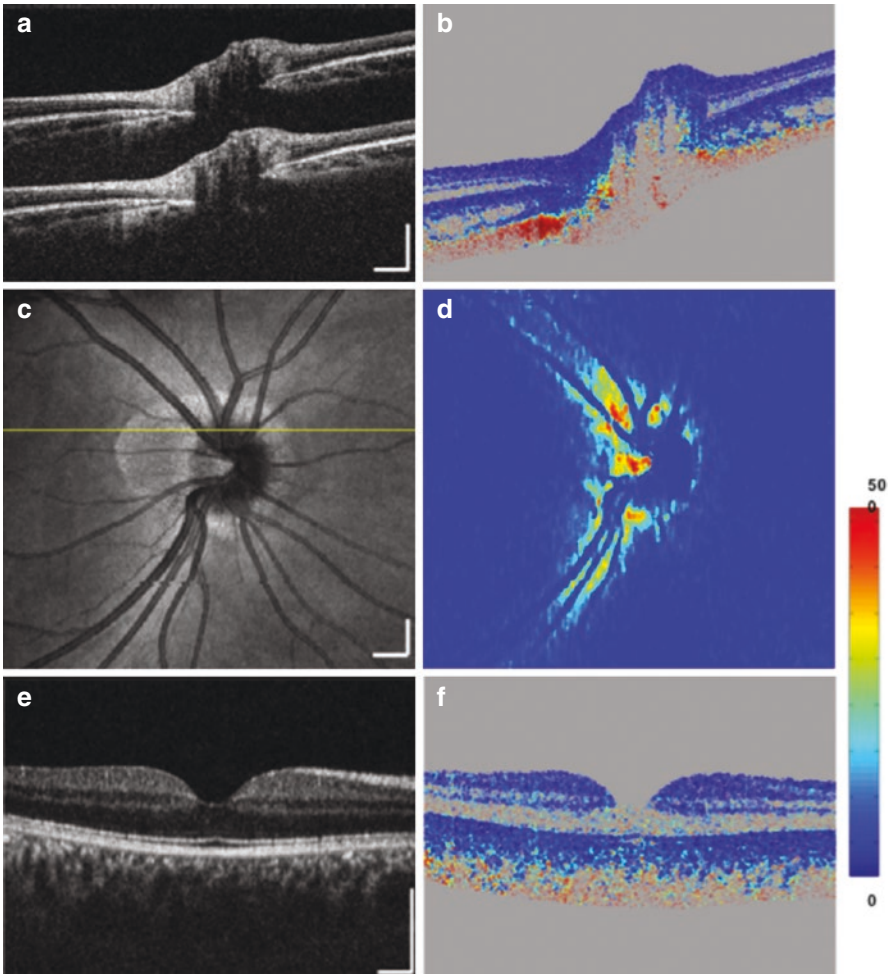

Fig. 2.14 PS-OCT optic nerve head and retinal imaging in healthy subjects. (**a**) A cross-sectional intensity image with two depth-encoded copies of the optic nerve head region. (**b**) Corresponding PS-OCT image shows high retardance in the RNFL and sclera. (**c**) OCT fundus image. (**d**) Corresponding PS-OCT map shows high retardance around the optic nerve head region. (**e**) A cross-sectional intensity image at the fovea region. (**f**) Corresponding PS-OCT image shows low retardance in the retinal layers

measuring intensity, retardation, and optic axis information, thus providing both tissue structural and functional information. The technology was initially incorporated into TD-OCT system, with subsequent introduction into all known OCT iterations such as SD-OCT [57], SS-OCT [30], and AO-OCT [58]. A few studies demonstrated that alteration in the polarization of ocular tissues might precede the occurrence of structural alteration, thus evaluation of the functional properties of the RNFL [59], sclera, and RPE [60] using PS-OCT technology could be an

attractive candidate for improving the detection of ocular pathologies such as glaucoma and age-related macular degeneration.

2.10 Phase Sensitive OCT

The Phase Sensitive OCT technique is able to provide in vivo information on micron scale movements or vibrations within the tissue [61]. The technology analyzes the phase information of the back-reflected light beam, which is typically ignored in conventional OCT systems. OCT phase imaging has been demonstrated with SD-OCT [62] and SS-OCT [63] technologies. Phase sensitive OCT offers the advantage of simultaneously assessing both the structural and functional information of the scanned tissue. The device has been shown to capture the retinal pigment epithelium layer, Henle's loop of the macula and retinal nerve fiber layer [64–67]. PS-OCT might be clinically useful in the context of glaucoma, AMD and potentially multiple sclerosis [64, 66, 68], but the clinical application is challenging because it is very sensitive to eye motion.

In conclusion, OCT has an important clinical role in the diagnosis of ocular diseases and in tracking changes overtime, leading to improved clinical management and better insight into pathophysiology of diseases. The constant enhancement of this technology ensures that clinicians will have an indispensable diagnostic tool in their armament.

References

1. Fujimoto JG, Brezinski ME, Tearney GJ, Boppart SA, Bouma B, Hee MR, et al. Optical biopsy and imaging using optical coherence tomography. Nat Med. 1995;1(9):970–2.
2. Fercher AF, Mengedoht K, Werner W. Eye-length measurement by interferometry with partially coherent light. Opt Lett. 1988;13(3):186–8.
3. Izatt JA, Hee MR, Swanson EA, Lin CP, Huang D, Schuman JS, et al. Micrometer-scale resolution imaging of the anterior eye in vivo with optical coherence tomography. Arch Ophthalmol. 1994;112(12):1584–9.
4. Potsaid B, Baumann B, Huang D, Barry S, Cable AE, Schuman JS, et al. Ultrahigh speed 1050nm swept source/Fourier domain OCT retinal and anterior segment imaging at 100,000 to 400,000 axial scans per second. Opt Express. 2010;18(19):20029–48.
5. Wieser W, Biedermann BR, Klein T, Eigenwillig CM, Huber R. Multi-megahertz OCT: high quality 3D imaging at 20 million A-scans and 4.5 GVoxels per second. Opt Express. 2010;18(14):14685–704.
6. Kocaoglu OP, Cense B, Jonnal RS, Wang Q, Lee S, Gao W, et al. Imaging retinal nerve fiber bundles using optical coherence tomography with adaptive optics. Vis Res. 2011;51(16):1835–44.
7. Lavinsky F, Lavinsky D. Novel perspectives on swept-source optical coherence tomography. Int J Retina Vitreous. 2016;2:25.
8. Kuroda HBM, Suzuki M, Yoneya S. A high speed three-dimensional spectral domain optical coherence tomography with <2 mc axial resolution using wide bandwidth femtosecond mode-locked laser. Appl Phys Lett. 2013;102(25):251102.
9. Unterhuber A, Povazay B, Hermann B, Sattmann H, Chavez-Pirson A, Drexler W. In vivo retinal optical coherence tomography at 1040 nm - enhanced penetration into the choroid. Opt Express. 2005;13(9):3252–8.

10. Yasuno Y, Hong Y, Makita S, Yamanari M, Akiba M, Miura M, et al. In vivo high-contrast imaging of deep posterior eye by 1-microm swept source optical coherence tomography and scattering optical coherence angiography. Opt Express. 2007;15(10):6121–39.
11. Hale GM, Querry MR. Optical constants of water in the 200-nm to 200-microm wavelength region. Appl Opt. 1973;12(3):555–63.
12. Fercher AF, Hitzenberger CK, Drexler W, Kamp G, Sattmann H. In vivo optical coherence tomography. Am J Ophthalmol. 1993;116(1):113–4.
13. Ahlers C, Schmidt-Erfurth U. Three-dimensional high resolution OCT imaging of macular pathology. Opt Express. 2009;17(5):4037–45.
14. Kim JS, Ishikawa H, Sung KR, Xu J, Wollstein G, Bilonick RA, et al. Retinal nerve fibre layer thickness measurement reproducibility improved with spectral domain optical coherence tomography. Br J Ophthalmol. 2009;93(8):1057–63.
15. Drexler W, Morgner U, Kartner FX, Pitris C, Boppart SA, Li XD, et al. In vivo ultrahigh-resolution optical coherence tomography. Opt Lett. 1999;24(17):1221–3.
16. Lim H, Jiang Y, Wang Y, Huang YC, Chen Z, Wise FW. Ultrahigh-resolution optical coherence tomography with a fiber laser source at 1 microm. Opt Lett. 2005;30(10):1171–3.
17. Huber R, Adler DC, Fujimoto JG. Buffered Fourier domain mode locking: unidirectional swept laser sources for optical coherence tomography imaging at 370,000 lines/s. Opt Lett. 2006;31(20):2975–7.
18. Yaqoob Z, Wu J, Yang C. Spectral domain optical coherence tomography: a better OCT imaging strategy. BioTechniques. 2005;39(6 Suppl):S6–13.
19. Shu X, Beckmann L, Zhang H. Visible-light optical coherence tomography: a review. J Biomed Opt. 2017;22(12):1–14.
20. Yi J, Wei Q, Liu W, Backman V, Zhang HF. Visible-light optical coherence tomography for retinal oximetry. Opt Lett. 2013;38(11):1796–8.
21. Huang D, Swanson EA, Lin CP, Schuman JS, Stinson WG, Chang W, et al. Optical coherence tomography. Science. 1991;254(5035):1178–81.
22. Schuman JS, Pedut-Kloizman T, Hertzmark E, Hee MR, Wilkins JR, Coker JG, et al. Reproducibility of nerve fiber layer thickness measurements using optical coherence tomography. Ophthalmology. 1996;103(11):1889–98.
23. Hee MR, Izatt JA, Swanson EA, Huang D, Schuman JS, Lin CP, et al. Optical coherence tomography of the human retina. Arch Ophthalmol. 1995;113(3):325–32.
24. Otani T, Kishi S, Maruyama Y. Patterns of diabetic macular edema with optical coherence tomography. Am J Ophthalmol. 1999;127(6):688–93.
25. Sanchez-Tocino H, Alvarez-Vidal A, Maldonado MJ, Moreno-Montanes J, Garcia-Layana A. Retinal thickness study with optical coherence tomography in patients with diabetes. Invest Ophthalmol Vis Sci. 2002;43(5):1588–94.
26. Medeiros FA, Zangwill LM, Bowd C, Weinreb RN. Comparison of the GDx VCC scanning laser polarimeter, HRT II confocal scanning laser ophthalmoscope, and stratus OCT optical coherence tomograph for the detection of glaucoma. Arch Ophthalmol. 2004;122(6):827–37.
27. Paunescu LA, Schuman JS, Price LL, Stark PC, Beaton S, Ishikawa H, et al. Reproducibility of nerve fiber thickness, macular thickness, and optic nerve head measurements using StratusOCT. Invest Ophthalmol Vis Sci. 2004;45(6):1716–24.
28. Kagemann L, Wollstein G, Wojtkowski M, Ishikawa H, Townsend KA, Gabriele ML, et al. Spectral oximetry assessed with high-speed ultra-high-resolution optical coherence tomography. J Biomed Opt. 2007;12(4):041212.
29. Srinivasan VJ, Wojtkowski M, Fujimoto JG, Duker JS. In vivo measurement of retinal physiology with high-speed ultrahigh-resolution optical coherence tomography. Opt Lett. 2006;31(15):2308–10.
30. Yamanari M, Makita S, Lim Y, Yasuno Y. Full-range polarization-sensitive swept-source optical coherence tomography by simultaneous transversal and spectral modulation. Opt Express. 2010;18(13):13964–80.

31. Wojtkowski M, Srinivasan V, Fujimoto JG, Ko T, Schuman JS, Kowalczyk A, et al. Three-dimensional retinal imaging with high-speed ultrahigh-resolution optical coherence tomography. Ophthalmology. 2005;112(10):1734–46.
32. Leung CK, Cheung CY, Weinreb RN, Qiu Q, Liu S, Li H, et al. Retinal nerve fiber layer imaging with spectral-domain optical coherence tomography: a variability and diagnostic performance study. Ophthalmology. 2009;116(7):1257–63, 63e1–2.
33. Asrani S, Rosdahl JA, Allingham RR. Novel software strategy for glaucoma diagnosis: asymmetry analysis of retinal thickness. Arch Ophthalmol. 2011;129(9):1205–11.
34. Tan O, Chopra V, Lu AT, Schuman JS, Ishikawa H, Wollstein G, et al. Detection of macular ganglion cell loss in glaucoma by Fourier-domain optical coherence tomography. Ophthalmology. 2009;116(12):2305–14 e1–2.
35. Tan O, Li G, Lu AT, Varma R, Huang D, Advanced Imaging for Glaucoma Study G. Mapping of macular substructures with optical coherence tomography for glaucoma diagnosis. Ophthalmology. 2008;115(6):949–56.
36. Belghith A, Medeiros FA, Bowd C, Liebmann JM, Girkin CA, Weinreb RN, et al. Structural change can be detected in advanced-glaucoma eyes. Invest Ophthalmol Vis Sci. 2016;57(9):OCT511–8.
37. Bowd C, Zangwill LM, Weinreb RN, Medeiros FA, Belghith A. Estimating optical coherence tomography structural measurement floors to improve detection of progression in advanced glaucoma. Am J Ophthalmol. 2017;175:37–44.
38. Kim KE, Park KH, Jeoung JW, Kim SH, Kim DM. Severity-dependent association between ganglion cell inner plexiform layer thickness and macular mean sensitivity in open-angle glaucoma. Acta Ophthalmol. 2014;92(8):e650–6.
39. Lavinsky F, Wu M, Schuman JS, Lucy KA, Liu M, Song Y, et al. Can macula and optic nerve head parameters detect glaucoma progression in eyes with advanced circumpapillary retinal nerve fiber layer damage? Ophthalmology. 2018;125(12):1907–12.
40. Keane PA, Ruiz-Garcia H, Sadda SR. Clinical applications of long-wavelength (1,000-nm) optical coherence tomography. Ophthalmic Surg Lasers Imaging. 2011;42(Suppl):S67–74.
41. Yasin Alibhai A, Or C, Witkin AJ. Swept source optical coherence tomography: a review. Curr Ophthalmol Rep. 2018;6:7–16.
42. Wang B, Nevins JE, Nadler Z, Wollstein G, Ishikawa H, Bilonick RA, et al. In vivo lamina cribrosa micro-architecture in healthy and glaucomatous eyes as assessed by optical coherence tomography. Invest Ophthalmol Vis Sci. 2013;54(13):8270–4.
43. Omodaka K, Maekawa S, An G, Tsuda S, Shiga Y, Takada N, et al. Pilot study for three-dimensional assessment of laminar pore structure in patients with glaucoma, as measured with swept source optical coherence tomography. PLoS One. 2018;13(11):e0207600.
44. Wang B, Lucy KA, Schuman JS, Sigal IA, Bilonick RA, Lu C, et al. Tortuous pore path through the glaucomatous lamina cribrosa. Sci Rep. 2018;8(1):7281.
45. Hou H, Moghimi S, Zangwill LM, Shoji T, Ghahari E, Penteado RC, et al. Macula vessel density and thickness in early primary open-angle glaucoma. Am J Ophthalmol. 2019;199:120–32.
46. Leitgeb RA, Werkmeister RM, Blatter C, Schmetterer L. Doppler optical coherence tomography. Prog Retin Eye Res. 2014;41:26–43.
47. Werkmeister RM, Dragostinoff N, Pircher M, Gotzinger E, Hitzenberger CK, Leitgeb RA, et al. Bidirectional Doppler Fourier-domain optical coherence tomography for measurement of absolute flow velocities in human retinal vessels. Opt Lett. 2008;33(24):2967–9.
48. Wang Y, Fawzi AA, Varma R, Sadun AA, Zhang X, Tan O, et al. Pilot study of optical coherence tomography measurement of retinal blood flow in retinal and optic nerve diseases. Invest Ophthalmol Vis Sci. 2011;52(2):840–5.
49. Liang J, Williams DR, Miller DT. Supernormal vision and high-resolution retinal imaging through adaptive optics. J Opt Soc Am A Opt Image Sci Vis. 1997;14(11):2884–92.
50. Roorda A, Romero-Borja F, Donnelly Iii W, Queener H, Hebert T, Campbell M. Adaptive optics scanning laser ophthalmoscopy. Opt Express. 2002;10(9):405–12.
51. Hermann B, Fernandez EJ, Unterhuber A, Sattmann H, Fercher AF, Drexler W, et al. Adaptive-optics ultrahigh-resolution optical coherence tomography. Opt Lett. 2004;29(18):2142–4.

52. Kocaoglu OP, Lee S, Jonnal RS, Wang Q, Herde AE, Derby JC, et al. Imaging cone photoreceptors in three dimensions and in time using ultrahigh resolution optical coherence tomography with adaptive optics. Biomed Opt Express. 2011;2(4):748–63.
53. Takayama K, Ooto S, Hangai M, Ueda-Arakawa N, Yoshida S, Akagi T, et al. High-resolution imaging of retinal nerve fiber bundles in glaucoma using adaptive optics scanning laser ophthalmoscopy. Am J Ophthalmol. 2013;155(5):870–81.
54. Burns SA, Tumbar R, Elsner AE, Ferguson D, Hammer DX. Large-field-of-view, modular, stabilized, adaptive-optics-based scanning laser ophthalmoscope. J Opt Soc Am A Opt Image Sci Vis. 2007;24(5):1313–26.
55. Zawadzki RJ, Choi SS, Fuller AR, Evans JW, Hamann B, Werner JS. Cellular resolution volumetric in vivo retinal imaging with adaptive optics-optical coherence tomography. Opt Express. 2009;17(5):4084–94.
56. Jonnal RS, Kocaoglu OP, Zawadzki RJ, Liu Z, Miller DT, Werner JS. A review of adaptive optics optical coherence tomography: technical advances, scientific applications, and the future. Invest Ophthalmol Vis Sci. 2016;57(9):OCT51–68.
57. Gotzinger E, Pircher M, Baumann B, Ahlers C, Geitzenauer W, Schmidt-Erfurth U, et al. Three-dimensional polarization sensitive OCT imaging and interactive display of the human retina. Opt Express. 2009;17(5):4151–65.
58. Cense B, Gao W, Brown JM, Jones SM, Jonnal RS, Mujat M, et al. Retinal imaging with polarization-sensitive optical coherence tomography and adaptive optics. Opt Express. 2009;17(24):21634–51.
59. Liu S, Wang B, Yin B, Milner TE, Markey MK, McKinnon SJ, et al. Retinal nerve fiber layer reflectance for early glaucoma diagnosis. J Glaucoma. 2014;23(1):e45–52.
60. Michels S, Pircher M, Geitzenauer W, Simader C, Gotzinger E, Findl O, et al. Value of polarisation-sensitive optical coherence tomography in diseases affecting the retinal pigment epithelium. Br J Ophthalmol. 2008;92(2):204–9.
61. Choma MA, Ellerbee AK, Yang C, Creazzo TL, Izatt JA. Spectral-domain phase microscopy. Opt Lett. 2005;30(10):1162–4.
62. Joo C, Akkin T, Cense B, Park BH, de Boer JF. Spectral-domain optical coherence phase microscopy for quantitative phase-contrast imaging. Opt Lett. 2005;30(16):2131–3.
63. Sarunic MV, Weinberg S, Izatt JA. Full-field swept-source phase microscopy. Opt Lett. 2006;31(10):1462–4.
64. Ju MJ, Hong YJ, Makita S, Lim Y, Kurokawa K, Duan L, et al. Advanced multi-contrast Jones matrix optical coherence tomography for Doppler and polarization sensitive imaging. Opt Express. 2013;21(16):19412–36.
65. Cense B, Wang Q, Lee S, Zhao L, Elsner AE, Hitzenberger CK, et al. Henle fiber layer phase retardation measured with polarization-sensitive optical coherence tomography. Biomed Opt Express. 2013;4(11):2296–306.
66. Braaf B, Vermeer KA, de Groot M, Vienola KV, de Boer JF. Fiber-based polarization-sensitive OCT of the human retina with correction of system polarization distortions. Biomed Opt Express. 2014;5(8):2736–58.
67. Wang Z, Lee HC, Ahsen OO, Lee B, Choi W, Potsaid B, et al. Depth-encoded all-fiber swept source polarization sensitive OCT. Biomed Opt Express. 2014;5(9):2931–49.
68. Jiang H, Chen W, Delgado S, Liu Y, Lin Y, Wang J. Altered birefringence of peripapillary retinal nerve fiber layer in multiple sclerosis measured by polarization sensitive optical coherence tomography. Eye Vis (Lond). 2018;5:14.